JOURNAL OF GEOPHYSICAL RESEARCH, VOL. 102, NO. D14, PAGES 16,407–16,422, JULY 27, 1997

Improved surface and boundary layer models for the Goddard Institute for Space Studies general circulation model

Gregory J. Hartke
Center for Climate Systems Research, Columbia University, New York

David Rind
Institute for Space Studies, NASA Goddard Space Flight Center, New York

Abstract. Improved surface and boundary layer models have been developed and implemented in the Goddard Institute for Space Studies (GISS) general circulation model (GCM). The new boundary layer model retains the methodology of the Model 2 version in which the surface winds are interpolated using a model profile but amends the approximations that were previously used to keep the model analytical for ease of computation. The new surface layer model is entirely different than that previously used in the GISS GCM and uses similarity theory to compute the transport coefficients, drag coefficient, Dalton number, and Stanton number. The combination yields distinct improvements in the general circulation characteristics of the GISS GCM. The new boundary layer and surface models were chosen to allow surface properties to be precomputed, resulting in minimal impact to the overall execution time. This is particularly important in a GCM used for climate experiments with timescales spanning centuries.

1. Introduction

The accurate depiction of climate using a general circulation model (GCM) requires a realistic representation of the physics of the atmospheric layer immediately adjacent to the planetary surface. It is through this planetary boundary layer (PBL) that the heat deposited on the Earth by the Sun enters the main body of the atmosphere. An important thermodynamic constituent of the atmosphere, water vapor, enters the atmosphere through evaporation from the surface and transport through the boundary layer. In addition, the PBL is the region in which a large fraction of the kinetic energy of the atmosphere is dissipated and through which vorticity exchange with the overlying atmospheric layers takes place. The depiction of the atmospheric boundary layer is thus of real import in the accurate prediction of surface quantities such as global precipitation patterns and surface wind, temperature, and humidity, and especially the surface fluxes of these quantities.

Current operational GCMs have a variety of PBL schemes [*Garratt*, 1993]. The most advanced of these have multiple layers in the PBL and use second-order turbulence closure schemes to compute the transport coefficients, fluxes, and prognostic quantities. Other GCMs use a first-order closure scheme in which the transport coefficients are specified as functions of a mixing length and a bulk Richardson number. These formulations typically have anywhere from one to four layers in the PBL. The Goddard Institute for Space Studies (GISS) Model 2 GCM [*Hansen et al.*, 1983] used a crude depiction of the PBL that relied on the interpolation of surface winds using an analytic Ekman model and a prescription for the transport coefficients based on bulk Richardson number to compute fluxes into the first model layer and the surface values of the prognostic variables. The original rationale for using such a simple scheme was to keep the computational demands small to facilitate numerical experiments extending over centuries of model time.

In order to maintain the low computational demands of the Model 2 PBL, the new scheme retains this methodology but improves the physics of the model components and parameterizations. There are two major components in the computation of the surface properties in the Model 2 PBL. First, a model is needed for the interpolation of the surface wind velocity. The parameters required in this model are the drag coefficient of the surface layer (c_m) and the turbulent viscosity (K_M) that characterizes the spiral layer. Second, the computation of the surface temperature is done by balancing the heat flux through the surface layer with that into the first model layer. This computation requires the Stanton number (c_h) of the surface layer and the turbulent diffusivity (K_H). The simultaneous solution of the equations of these two PBL model components determines all surface values of the prognostic variables as well as the fluxes of momentum, heat, and moisture.

1.1. Deficiencies of the Model 2 PBL

The major deficiency of the Model 2 PBL was that the approximations used to render the equations for the wind velocity profile analytically tractable yielded a model that did not have physically acceptable solutions at the equator for the boundary conditions imposed on the flow and remained inapplicable at low latitudes. The upper boundary condition used in the old model was that the wind profile become smooth (i.e., was specified to have vanishing second derivative) when the ratio of boundary layer height to Ekman length was large (>2 or 3 in practice). However, the Ekman length has a factor of

Paper number 97JD00698.
0148-0227/97/97JD-00698$09.00

inverse sine latitude, causing divergence at the equator. Thus the upper boundary condition on the flow could never be met in the physical regime, requiring that the ratio of the height of the boundary layer to the radius of the Earth be small. This was a consequence of the use of a semi-infinite solution domain for the model velocity profile. For this domain, the only relevant length scale was the Ekman length.

Second, the drag coefficient and Stanton number were parameterized in terms of a simple bulk Richardson number characterizing the surface layer. These quantities would be more realistically represented in terms of complicated functions of the momentum and heat fluxes determined by the type of topography present in the underlying grid box. The type of parameterization used in Model 2, while computationally simple, could not possibly capture the proper scaling for all possible atmospheric conditions. Similarly, a crude bulk parameterization was also used for the turbulent transport coefficient, and no distinction was made between the transport coefficients for heat, momentum, and moisture. Comparison with the results of a one-dimensional (1-D) off-line Reynolds stress closure model (constructed from that of *Galperin et al.* [1988]) indicated that the transport coefficients were typically overestimated by at least an order of magnitude in Model 2, leading to insufficient wind turning from top to bottom of the boundary layer and poor estimates of the surface fluxes and values of the prognostic variables.

There were also other internal inconsistencies in the Model 2 PBL, such as a parameterization of the roughness length over ocean and, independently, a parameterized neutral drag coefficient over ocean. In reality, a clear relationship exists between the two. (See section 4.)

1.2. Improvements in the New PBL

The new PBL is designed to minimize the use of empirical parameterizations that were previously adopted on the basis of numerical simplicity. These types of parameterizations can obscure scalings that could be important in a GCM. All choices for any free parameters in the model were made through comparison of the results of an off-line version of the new PBL model with parameterized results of the Wangara experiment [*Yamada*, 1976]. A 1-D simulation using a level $2\frac{1}{2}$ Reynolds stress closure model [*Galperin et al.*, 1988] was also used to help define the physics of the new PBL model. At no time was the model tweaked or tuned purely on the basis of GCM test runs.

The new model for the wind velocity profile uses, as in Model 2, a modified Ekman model characterized by constant turbulent viscosity. Here, though, the model equations are solved on a finite domain, the upper boundary being the height of the boundary layer. This model now correctly gives purely pressure gradient–driven flow at the equator in the appropriate limit and allows for a realistic wind spiral without recourse to the addition of a thermal wind, as was done in Model 2. The trade-off for the improvement in the wind profile interpolation is that the model can no longer be completely solved analytically.

The turbulent transport coefficients, K_M and K_H, are computed in the new model using similarity theory. Similarity theory is a hypothesis of Monin and Obukhov (see, for example, *Monin and Yaglom* [1971]) that any dimensionless characteristic of the turbulence in the surface layer can depend only on the surface friction speed, the altitude, the ratio g/T_v (g is the acceleration due to gravity and T_v is the virtual potential temperature), and the surface buoyancy flux. The turbulent diffusivity, K_H, appears in the expression for the heat flux into the first layer and is evaluated at the height of the surface layer. The turbulent viscosity, K_M, appearing in the model equations for the velocity profile, is taken to be constant and is computed at a fixed fraction of the boundary layer height.

Similarity theory is also used to specify the instability functions that determine the drag coefficient and Stanton number. In addition, the Dalton number (c_q) is now taken to be distinct from the Stanton number and is also computed using similarity theory.

Ocean and ocean ice are now treated as rough surfaces for which the roughness lengths z_{0m}, z_{0h}, z_{0q} are specified as functions of momentum flux and are used to compute the neutral drag coefficient, Stanton number, and Dalton number. The roughness lengths are particularly important because the fluxes are strongly dependent on the neutral coefficients.

The temperature gradient used to compute the heat flux into the first model layer is more accurately computed in the new model. In Model 2 the gradient used to compute the buoyancy flux into the first model layer was approximated by the virtual potential temperature difference between the surface and first layer divided by the difference in altitude between the surface and first layer. However, simulations using a second-order closure model indicated that the typical profile of atmospheric virtual potential temperature has a varying surface layer overlain by a well-mixed layer of approximately constant virtual potential temperature. The height of the bottom of this mixed layer is usually at a considerably lower altitude than the mean of the first model layer. In the new model the height of the bottom of this mixed layer is found by computing the altitude at which the temperature gradient predicted using similarity theory becomes small. This allows (in a limited fashion) subgrid scale resolution of the region in which the temperature gradient is appreciable and a more accurate computation of the temperature gradient and buoyancy flux. This same method is used to compute the surface moisture gradient, and hence the surface moisture.

There are caveats to the approach used in this model. The scaling of similarity theory is fairly well verified except at the extremes of stability. The instability functions used in similarity theory are empirically determined, so the model should be updated as better experimental information becomes available. The small stress regime of the roughness lengths is fairly well established theoretically; however, the large stress asymptotes are a bit more problematical. Again, attention must be kept on future developments in this area. The greatest difficulty in conjunction with the new velocity profile and the use of similarity theory with its complex scaling behavior is that payment must be made in CPU time: The model is somewhat computationally intensive due to the required nested iterations. Thus a precomputed version of this PBL model was developed that introduced still another layer of approximation. In this version of the model, the full computation of the PBL properties is only done if the determining quantities are beyond the limits of the precomputed table. Off-line and on-line testing of a precomputed version of this PBL model was entirely satisfactory, and it is this version which is incorporated into the current version of the GISS GCM. The result is that even with the improvement in the physics of the PBL, the GISS GCM with the precomputed PBL runs approximately 5–10% faster than Model 2.

2. The Model Velocity Profile

The original GISS GCM Model 2 used an analytic wind profile developed by *Taylor* [1915, 1916]. The new wind profile is computed from the same model equations as Model 2, i.e., a barotropic PBL is assumed characterized by constant eddy viscosity K_M, but the new model computes the wind profile on a finite domain of height H, the height of the PBL. Since the PBL height is small compared to the radius of the Earth, choose a locally Cartesian coordinate system oriented such that x increases eastward, y increases northward, and z increases radially outward. The equations determining the mean velocity field are then [*Pedlosky*, 1979]

$$-\frac{1}{\rho}\frac{\partial P}{\partial x} + 2\Omega_3 U_2 + K_M \frac{d^2U_1}{dz^2} = 0 \tag{1}$$

$$-\frac{1}{\rho}\frac{\partial P}{\partial y} - 2\Omega_3 U_1 + K_M \frac{d^2U_2}{dz^2} = 0, \tag{2}$$

where ρ is the density, P is the pressure, $\Omega_3 = \Omega \sin \lambda$ with Ω the angular frequency of the Earth and λ the latitude, K_M is the turbulent viscosity, U_1 is the x component of the mean wind, and U_2 is the y component of the mean wind.

The upper boundary condition applied to the solutions of (1) and (2) is, as in the work by *Pedlosky* [1979], that the mean wind go smoothly into the wind above the boundary layer, i.e.,

$$\left.\frac{d\mathbf{U}}{dz}\right|_H = 0. \tag{3}$$

The lower boundary condition is determined by the requirement that the Reynolds stress $\boldsymbol{\tau}$, given in general by

$$\boldsymbol{\tau} = -\rho K_M \frac{d\mathbf{U}}{dz}, \tag{4}$$

be continuous between the surface layer and the boundary layer. At the top of the surface layer, a drag law parameterization is used to represent the stress,

$$\boldsymbol{\tau}(z_s) = -\rho c_m U(z_s)\mathbf{U}(z_s), \tag{5}$$

where c_m is the drag coefficient and $z_s = 10$ m is the height of the surface layer in the GCM. Continuity of the stress at the surface height z_s then gives

$$K_M \left.\frac{d\mathbf{U}}{dz}\right|_{z_s} = c_m U(z_s)\mathbf{U}(z_s) \tag{6}$$

as the boundary condition at the bottom of the boundary layer to be applied to the solutions of (1) and (2).

In the northern hemisphere, the solutions of (1) and (2) that satisfy the upper boundary condition (3) are

$$\hat{U}_1(\zeta) = \cos\theta + a(\cosh k\zeta \cos k\zeta - 1) - b \sinh k\zeta \sin k\zeta \tag{7}$$

$$\hat{U}_2(\zeta) = \sin\theta + a \sinh k\zeta \sin k\zeta + b(\cosh k\zeta \cos k\zeta - 1), \tag{8}$$

where $\hat{U}_1$ and $\hat{U}_2$ are the x and y components of the mean wind, respectively, divided by U_0, the wind speed at the top of the boundary layer, $\zeta = (z - H)/(H - z_s)$, θ is the direction of the mean wind at the top of the boundary layer, the quantity k is given by

$$k^2 = [\Omega(H - z_s)^2/K_M] \sin\lambda, \tag{9}$$

and a and b are integration constants. All solutions in the boundary layer are computed as if in the northern hemisphere and rotated appropriately for grid points in the southern hemisphere. In the GISS GCM the boundary layer height is taken to be the height of the layer to which dry convection mixed at the previous time step for unstable conditions and $H = 0.15u_*/\Omega$ for stable conditions. The vertical resolution of the GISS GCM (nine vertical levels) provides a clear limitation in the accurate specification of the wind at the top of the boundary layer. This problem will be addressed in future versions of the model in which significant improvements in vertical resolution are planned.

Application of the lower boundary condition represented by (6) in a coordinate system rotated such that the y component of the surface wind vanishes yields

$$c_4\hat{a}^4 + c_3\hat{a}^3 + c_2\hat{a}^2 + c_1\hat{a} + c_0 = 0, \tag{10}$$

to be solved for $\hat{a}$ where

$$c_4 = (\alpha_1^2 + \beta_1^2)^2(\alpha_2^2 + \beta_2^2)^2 \tag{11}$$

$$c_3 = \frac{2k}{c_m R}(\alpha_2^2 + \beta_2^2)[(\alpha_1^2 - \beta_1^2)(\alpha_2^2 - \beta_2^2) + 4\alpha_1\alpha_2\beta_1\beta_2] \tag{12}$$

$$c_2 = \frac{k^2}{c_m^2 R^2}(\alpha_2^2 + \beta_2^2)^2 - 2(\alpha_1^2 + \beta_1^2)(\alpha_2^2 + \beta_2^2) \tag{13}$$

$$c_1 = \frac{2k}{c_m R}(\alpha_2^2 + \beta_2^2) \tag{14}$$

$$c_0 = 1 \tag{15}$$

with Reynolds number $R = U_0(H - z_s)/K_M$ and

$$\alpha_1 = e^{-k}[\cosh k \cos k - 1] \tag{16}$$

$$\beta_1 = e^{-k} \sinh k \sin k \tag{17}$$

$$\alpha_2 = e^{-k}[\sinh k \cos k - \cosh k \sin k] \tag{18}$$

$$\beta_2 = e^{-k}[\sinh k \cos k + \cosh k \sin k]. \tag{19}$$

The integration constants a and b are related to $\hat{a}$ by

$$a = e^{-k}(\alpha_2 \cos\phi + \beta_2 \sin\phi)\hat{a} \tag{20}$$

$$b = e^{-k}\frac{\beta_2 \cos\phi - \alpha_2 \sin\phi}{\alpha_2 \cos\phi - \beta_2 \sin\phi}\hat{a}. \tag{21}$$

The angle $\phi = \theta + \gamma$, where γ is the angle through which the wind spirals from the top to the bottom of the boundary layer, is given by

$$\sin\gamma = (\alpha_2\beta_1 - \alpha_1\beta_2)\hat{a}. \tag{22}$$

The dimensionless surface wind speed is then given by

$$\hat{U}(z_s) = \cos\gamma + (\alpha_1\alpha_2 + \beta_1\beta_2)\hat{a} \tag{23}$$

and the dimensionless components of the surface wind by

$$\hat{U}_1(z_s) = \hat{U}(z_s)\cos\phi \tag{24}$$

$$\hat{U}_2(z_s) = \hat{U}(z_s)\sin\phi. \tag{25}$$

The physically correct solution for (10) is the one for which $\hat{a}$ is purely real and for which

$$0 \le \hat{U}(z_s) \le 1 \tag{26}$$

along with

$$0 \le \gamma \le \pi/4. \tag{27}$$

The upper limit on γ can be established analytically by considering the limit $K_M \to 0$ of (11)–(23). This is the zero friction limit for which there is maximum spiraling of the wind from top to bottom of the boundary layer.

3. Transport Coefficients and Fluxes Into the First Model Layer

As in Model 2 the fluxes of sensible heat and water vapor in the surface layer are computed using

$$F_h = c_p \rho c_h U(z_s)[T(z_s) - T(z_{0h})] \tag{28}$$

$$F_q = \rho c_q U(z_s)[q(z_s) - q(z_{0q})], \tag{29}$$

where F_h and F_q are the fluxes of sensible heat and water vapor, respectively, c_p is the specific heat at constant pressure, c_h is the Stanton number, c_q is the Dalton number, T is the virtual potential temperature, q is the water vapor mixing ratio, and z_{0h} and z_{0q} are the roughness lengths for temperature and moisture, respectively. The temperature and moisture mixing ratio at the height of the appropriate roughness length are actually the ground values (T_G and Q_G) of these fields. In Model 2, T_G is computed from the balance between net radiation, latent and sensible heat fluxes (equations (28) and (29)), and heat conduction in the ground. (For details, see *Hansen et al.* [1983].) Q_G is the saturated value of the ground moisture mixing ratio at T_G and is computed via the Clausius-Clapeyron equation.

Also as in Model 2 the fluxes into the first layer are computed using

$$F_h = c_p \rho K_H \left.\frac{dT}{dz}\right|_{z_s} \tag{30}$$

$$F_q = \rho K_q \left.\frac{dq}{dz}\right|_{z_s} \tag{31}$$

where K_q is the transport coefficient for water vapor. In Model 2 it was assumed that $K_q = K_H = K_M$ as well as $c_q = c_h$.

Detailed second-order closure (SOC) model computations depict the thermal structure of the simulation domain as a well-mixed layer of nearly constant temperature atop a narrow region of strong temperature gradient. The bottom of the mixed layer was generally significantly lower than the height of the first model layer (≈200 m) in the GCM. The SOC model results demonstrated that a good numerical approximation to the gradients of temperature and water vapor in the PBL model was

$$\left.\frac{dT}{dz}\right|_{z_s} \approx \frac{T_1 - T(z_s)}{z_{\text{mix}} - z_s} \tag{32}$$

$$\left.\frac{dq}{dz}\right|_{z_s} \approx \frac{q_1 - q(z_s)}{z_{\text{mix}} - z_s}, \tag{33}$$

where the subscript 1 denotes the first model layer. Equations (32) and (33) introduce z_{mix}, the altitude of the bottom of the mixed layer, determined by finding the height at which the temperature gradient predicted by similarity theory is small compared to the gradient at the surface. Clearly, $z_{\text{mix}} \le z_1$ (≈200 m), since if z_{mix} were greater than z_1, the temperature and moisture gradients would be adequately approximated by $z_{\text{mix}} = z_1$.

Equating (28) and (32) leads to an implicit equation for the surface temperature, $T(z_s)$. This equation, which balances the flux in the surface layer with that into the first model layer, is solved simultaneously with that for the momentum flux which determines the wind profile. (See (44) below.) Since the surface temperature is known, (29) and (33) are then combined and solved for the water vapor mixing ratio. The surface wind, surface temperature, and surface mixing ratio are then known along with the accompanying fluxes of momentum, specific heat, and water vapor.

The new PBL model uses similarity theory to compute the transport coefficients, given by

$$K_M(z) = \frac{\kappa u_* z}{\phi_M(z/L)} \tag{34}$$

$$K_H(z) = \frac{\kappa u_* z}{\phi_H(z/L)}, \tag{35}$$

where ϕ_M and ϕ_H are the dimensionless velocity and temperature gradients, respectively, $\kappa = 0.40$ is the von Karman constant, $u_*^2 = c_m U^2(z_s)$ where u_* is the friction speed, and $L = c_p \rho u_*^3 T(z_s)/\kappa g F_h$ is the Monin-Obukhov length scale. Expressions for the dimensionless gradients were taken from the analysis of available experimental data by *Hogstrom* [1988]:

$$\phi_M(\xi) = (1 - \gamma_M \xi)^{-1/4} \qquad \xi < 0 \tag{36}$$

$$\phi_H(\xi) = \sigma_T (1 - \gamma_H \xi)^{-1/2} \qquad \xi < 0 \tag{37}$$

$$\phi_M(\xi) = 1 + \beta_M \xi \qquad \xi \ge 0 \tag{38}$$

$$\phi_H(\xi) = \sigma_T (1 + \beta_H \xi) \qquad \xi \ge 0 \tag{39}$$

where $\sigma_T = 0.95$ is the turbulent Prandtl number at neutrality and

$$\gamma_M = 19.3 \tag{40}$$

$$\gamma_H = 11.6 \tag{41}$$

$$\beta_M = 4.8 \tag{42}$$

$$\beta_H = 8/\sigma_T. \tag{43}$$

The dimensionless gradients for water vapor have been taken to be the same as those for temperature, and the assumption that $K_q = K_H$ is retained. This is the simplest procedure, and as yet there is no compelling evidence to the contrary.

K_H is computed using (35) at the height of the surface layer, z_s. The altitude at which to compute K_M is more problematical. The model used to compute the wind profile assumes that K_M is constant with altitude, when it is obvious that it is not. The point of view adopted here is that the eddy viscosity used in the wind model is a value that characterizes the boundary layer as a whole and acts to provide the friction that reduces the turning of the wind from top to bottom. (The turning angle would be $\pi/4$ for vanishing eddy viscosity.) For simplicity, the eddy viscosity is computed at a fixed fraction f of the PBL height. The fraction f was fixed by comparing wind-turning angles computed using the off-line PBL model with those of *Yamada* [1976] under a large variety of atmospheric conditions. The turning was not terribly sensitive to f, which was fixed at $f = 0.1$.

4. The Surface Layer Parameterization

As in Model 2 the flux of momentum in the surface layer is computed using a drag law parameterization

$$\tau = -\rho c_m U(z_s)\mathbf{U}(z_s) \tag{44}$$

and the fluxes of sensible heat and water vapor are given by (28) and (29). The initial version of the new PBL scheme updated the Model 2 version through the use of new semiempirical expressions for the drag coefficient and Dalton number (bulk expressions similar to those of Model 2) and assumed $c_q = c_h$. Off-line testing of the new PBL scheme and comparison with the results of *Yamada* [1976] demonstrated that the fluxes were very sensitive to the chosen values of these coefficients. In essence, the magnitudes of the surface fluxes were strongly determined by c_m and c_h, while the surface quantities (surface temperature and wind) were strongly determined by the transport coefficients. This can be understood by equating, for example, (28) with the right-hand side of (30) using (32). Clearly, the magnitude of the flux is strongly influenced by the value of c_h. The surface temperature then adjusts, yielding a consistent result. Given this sensitivity, the importance of the drag coefficient, Dalton number, and Stanton number become apparent. It is thus necessary to specify these coefficients as accurately as possible, and the semiempirical expressions previously used were deemed not sufficiently accurate.

Using similarity theory, quite general expressions can be derived for the drag coefficient, Dalton number, and Stanton number. These quantities are given by

$$c_m = c_{mn}\Gamma_m \tag{45}$$

$$c_h = c_{hn}\Gamma_h \tag{46}$$

$$c_q = c_{qn}\Gamma_q \tag{47}$$

where the subscript n denotes neutral stability in

$$c_{mn} = \frac{\kappa^2}{(\ln z_s/z_{0m})^2} \tag{48}$$

$$c_{hn} = \frac{\kappa^2}{(\ln z_s/z_{0m})(\ln z_s/z_{0h})} \tag{49}$$

$$c_{qn} = \frac{\kappa^2}{(\ln z_s/z_{0m})(\ln z_s/z_{0q})}, \tag{50}$$

and the factors

$$\Gamma_m = \left[1 - \frac{1}{\ln z_s/z_{0m}}(\psi_m(z_s/L) - \psi_m(z_{0m}/L))\right]^{-2} \tag{51}$$

$$\Gamma_h = \Gamma_m^{1/2}\left[1 - \frac{1}{\ln z_s/z_{0h}}(\psi_h(z_s/L) - \psi_h(z_{0h}/L))\right]^{-1} \tag{52}$$

$$\Gamma_q = \Gamma_m^{1/2}\left[1 - \frac{1}{\ln z_s/z_{0q}}(\psi_q(z_s/L) - \psi_q(z_{0q}/L))\right]^{-1} \tag{53}$$

correct the neutral coefficients for stability. In (51)–(53) the ψ functions are antiderivatives of particular functions of the ϕ

$$\psi_i(\chi) = \int^{\chi} dy\, \frac{1 - \phi_i(y)}{y} \tag{54}$$

with the index i denoting m, h, or q. For the dimensionless gradients given by (36)–(39), the indicated integrals in (54) are easily done analytically with the result

$$\Delta\psi_m = \ln\frac{(1 + x_m)^2(1 + x_m^2)}{(1 + x_{m0})^2(1 + x_{m0}^2)} - 2(\tan^{-1}x_m - \tan^{-1}x_{m0}) \qquad \frac{z_s}{L} < 0 \tag{55}$$

$$\Delta\psi_m = -\beta_m\frac{z_s - z_{0m}}{L} \qquad \frac{z_s}{L} \geq 0 \tag{56}$$

$$\Delta\psi_h = (1 - \sigma_T)\ln\frac{z_s}{z_{0h}} + 2\sigma_T\ln\frac{1 + x_h}{1 + x_{h0}} \qquad \frac{z_s}{L} < 0 \tag{57}$$

$$\Delta\psi_h = (1 - \sigma_T)\ln\frac{z_s}{z_{0h}} - \sigma_T\beta_h\frac{z - z_{0h}}{L} \qquad \frac{z_s}{L} > 0 \tag{58}$$

where $\Delta\psi_m \equiv \psi_m(z_s/L) - \psi_m(z_{0m}/L)$ and $\Delta\psi_h \equiv \psi_h(z_s/L) - \psi_h(z_{0h}/L)$. As before, z_{0m}, z_{0h}, and z_{0q} are the roughness lengths for momentum, temperature, and water vapor and

$$x_m = \left[1 - \gamma_m\frac{z_s}{L}\right]^{1/4} \tag{59}$$

$$x_h = \left[1 - \gamma_h\frac{z_s}{L}\right]^{1/2}. \tag{60}$$

The quantities x_{m0} and x_{h0} are obtained by replacing z_s in (59) and (60) by z_{0m} and z_{0h}. $\Delta\psi_q$ is obtained from $\Delta\psi_h$ by replacing z_{0h} by z_{0q}.

It remains to determine the roughness lengths to complete the specification of the dimensionless surface fluxes. Over land, z_{0m} is specified as in Model 2 [*Hansen et al.*, 1983]. The roughness length for temperature over land is taken from *Brutsaert* [1982] with $z_{0q} = z_{0h} = e^{-2}z_{0m}$. The roughness lengths over land ice use the same formulation as over land. Ocean and ocean ice are treated as rough bluff surfaces, with the roughness length for momentum combining the smooth surface value [*Brutsaert*, 1982] with the Charnock relation for the aerodynamic roughness length as

$$z_{0m} = \frac{\nu_m}{u_*} + 0.018\frac{u_*^2}{g}, \tag{61}$$

where $\nu_m = 0.135\nu$ and $\nu = 1.5 \times 10^{-5}$ m^2 s^{-1} is the viscosity of air. For ocean and ocean ice, the roughness lengths are again taken from *Brutsaert* [1982] with

$$z_{0h} = \nu_h/u_* \qquad u_* \leq 0.02 \text{ m/s} \tag{62}$$

$$z_{0q} = \nu_q/u_* \qquad u_* \leq 0.02 \text{ m/s} \tag{63}$$

$$z_{0h} = (1 - \eta)\frac{\nu_h}{u_*} + \eta\hat{z}_{0h} \qquad 0.02 < u_* < 0.2 \text{ m/s} \tag{64}$$

$$z_{0q} = (1 - \eta)\frac{\nu_q}{u_*} + \eta\hat{z}_{0q} \qquad 0.02 < u_* < 0.2 \text{ m/s} \tag{65}$$

$$z_{0h} = \hat{z}_{0h} \qquad u_* \geq 0.2 \text{ m/s} \tag{66}$$

$$z_{0q} = \hat{z}_{0q} \qquad u_* \geq 0.2 \text{ m/s} \tag{67}$$

where $\nu_h = 0.395\nu$, $\nu_q = 0.624\nu$, $\eta = (u_* - 0.02)/0.18$ (with u_* in meters per second),

$$\hat{z}_{0h} = 7.4z_{0m}\exp(-2.4604R_0^{1/4}) \tag{68}$$

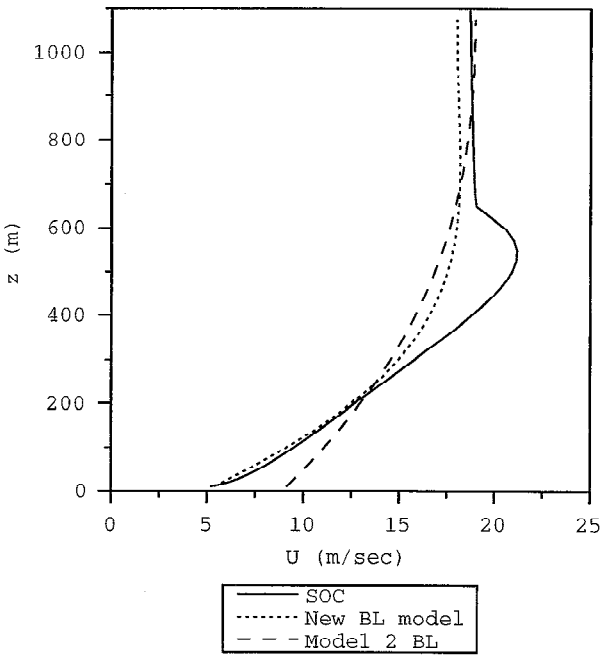

Figure 1a. The profile of the x component of the wind, U, at hour 3 of the simulation under stable conditions. The results depicted were computed using the SOC model, the new BL model, and the Model 2 BL model in the off-line simulation.

$$\hat{z}_{0q} = 7.4 z_{0m} \exp(-2.2524 R_0^{1/4}), \tag{69}$$

and

$$R_0 = u_* z_{0m}/\nu \tag{70}$$

is a roughness Reynolds number.

5. Off-Line Model Comparisons

Off-line versions of the new boundary layer (BL) model and the GCM Model 2 BL were constructed to illustrate the differences in profiles and fluxes computed using the two models. To provide a baseline against which the results from these two models can be compared, a simulation was prepared using the SOC model of *Galperin et al.* [1988] at level 2. The simulation domain for the SOC, defined as $z \in [10,3000]$ m, sits atop the surface layer presented in section 4. The lower boundary conditions on the wind and temperature fields were the same as for the new BL model, (6) for the wind and (28) and (30) for the temperature, with the field gradients computed between the lowest two levels of the SOC simulation domain. For simplicity, the wind at the top of the SOC simulation domain was prescribed as a constant 18 m/s in the x direction (i.e., due east), and the temperature gradient at the top was set to zero. The ground temperature was prescribed to vary with a period of 1 day. The maximum ground temperature was 290 K (at hour 15), and the minimum was 276.95 K (at hour 7). The phase of the temperature variation was such that hour 0 represented midnight. The SOC model used a log-linear grid scheme to enhance the resolution at the lower levels where the gradients of the prognostic fields are strongest. The simulation presented here used 128 grid points on the simulation domain. The terrain was specified as dry land and the momentum roughness length was specified as $z_{0m} = 0.1$ m. The simulation was done at a latitude of 40°N.

The SOC simulation was initiated with prescribed fields which were time advanced for 30 days under the periodic boundary conditions. After 30 days, the simulation was fully equilibriated, and the solutions were virtually perfectly periodic. The results presented here are taken from the final 24 hours of the 30 day simulation.

The new BL model and the Model 2 BL both require that the temperature at the first GCM model level be specified. In the GISS GCM, this is at a height of 200 m. Thus when the SOC simulation was run, the ground temperature and the temperature at 200 m were written to a data file hourly for the final 24 hours to provide boundary conditions for the off-line models. The Model 2 BL is completely insensitive to the boundary layer height, unlike the new BL model. In the GISS GCM the BL height is specified as $H = 0.15 u_*/\Omega$ for stable conditions and the height to which dry convection mixes at the previous time step for unstable conditions. The value of H for stable conditions was taken over verbatim from the GCM, but H for unstable conditions was more problematic. For simplicity, the same expression for H was adopted for both stable and unstable conditions. Scrutiny of the SOC simulation results indicated that this was a reasonable choice, and the value of H was saved to a data file hourly during the last 24 hours of the SOC simulation and used with the off-line BL models.

Representative results are given here for the stable conditions at hour 3 and for the unstable conditions at hour 15 of the final simulation day. Wind profiles are presented in Figures 1a and 1b for U and V, respectively, at hour 3 and in Figures 2a and 2b at hour 15. The diurnal variation of the computed surface winds are presented in Figure 3, and the diurnal variation of the fluxes of sensible heat and momentum at the surface are presented in Figures 4 and 5. A comparison of the numerical values of certain important quantities can be found in Table 1 for hour 3 and Table 2 for hour 15. The transport coefficients listed for the SOC results in Tables 1 and 2 are computed at a height of $0.1H$ for K_M and at the surface for K_H

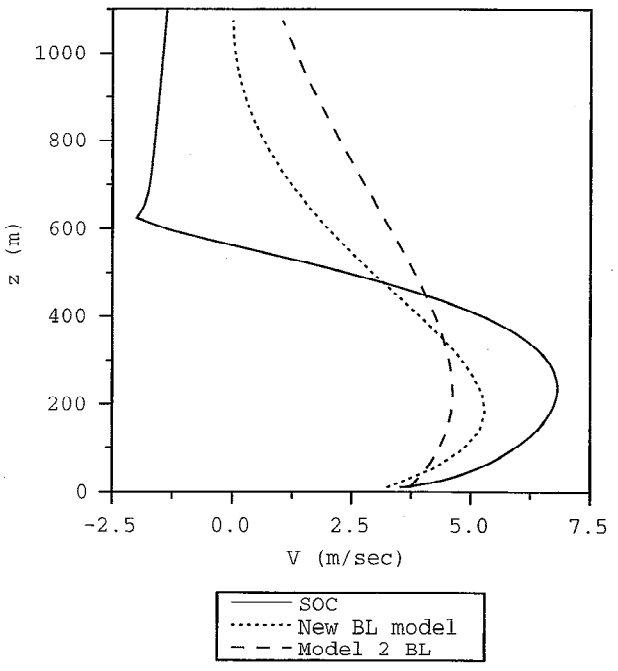

Figure 1b. As in Figure 1a, but for the y component of the wind, V.

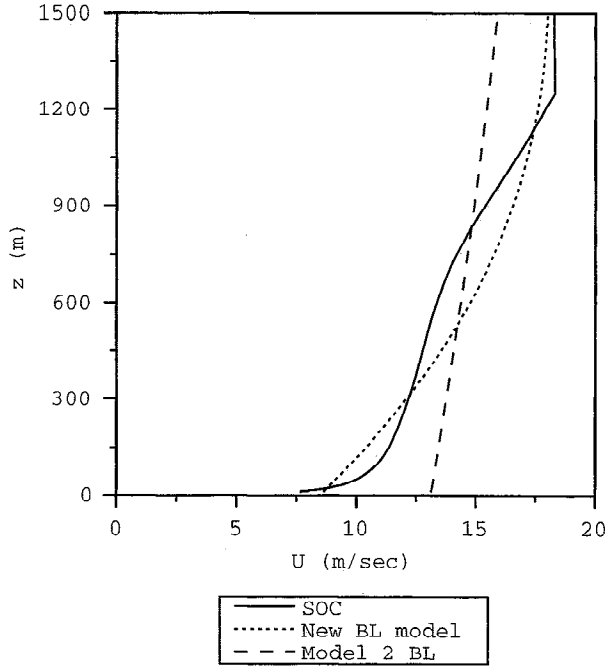

Figure 2a. The profile of the x component of the wind, U, at hour 15 of the simulation under unstable conditions. The results depicted were computed using the SOC model, the new BL model, and the Model 2 BL model in the off-line simulation.

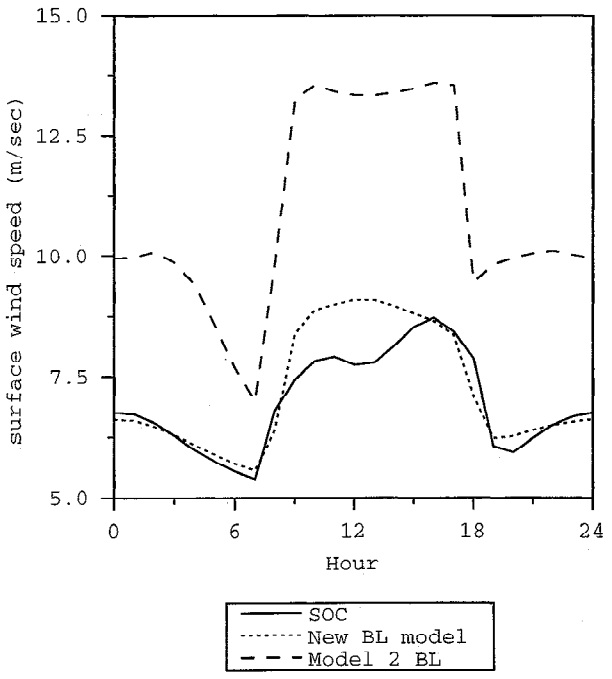

Figure 3. The diurnal variation of the surface wind computed using the SOC model, the new BL model, and the Model 2 BL model in the off-line simulation.

so that these values can be directly compared to the off-line model results. The wind-turning values listed in the tables are the amount that the wind has turned from the direction at the defined top of the boundary layer.

Several conclusions are immediately obvious. Under stable conditions the new BL model matches the SOC results reasonably well, doing a good job with both the magnitude and direction of the surface winds as well as the fluxes. Under unstable conditions the magnitude of the surface wind from the new BL model is not quite as good as under stable conditions but is considerably improved from the Model 2 BL, for which it is consistently overestimated. This is true for the fluxes under unstable conditions as well.

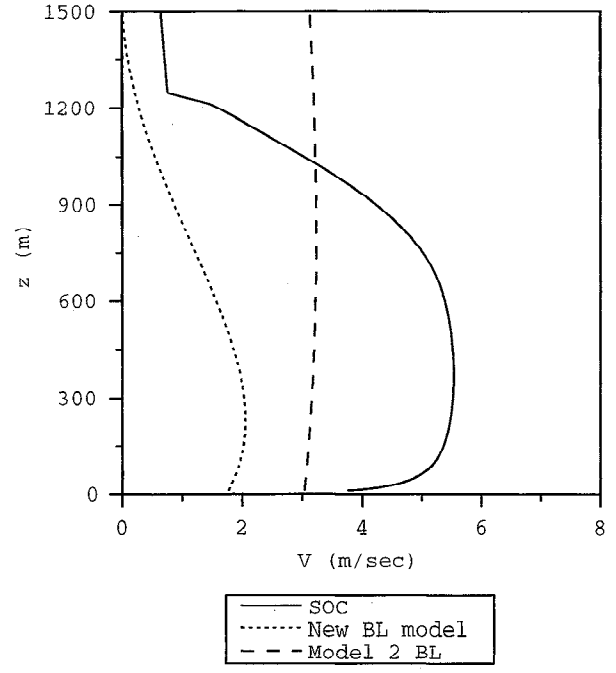

Figure 2b. As in Figure 2a, but for the y component of the wind, V.

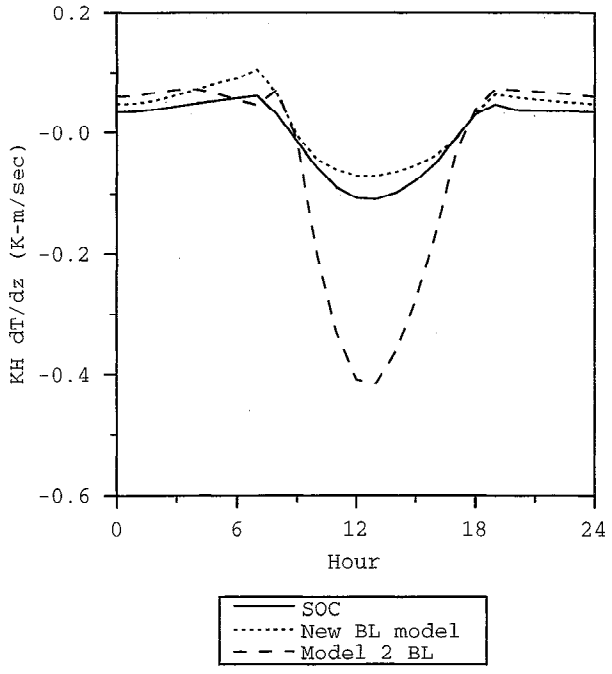

Figure 4. The diurnal variation of the flux of sensible heat, $K_H\, dT/dz$, at the surface computed using the SOC model, the new BL model, and the Model 2 BL model in the off-line simulation.

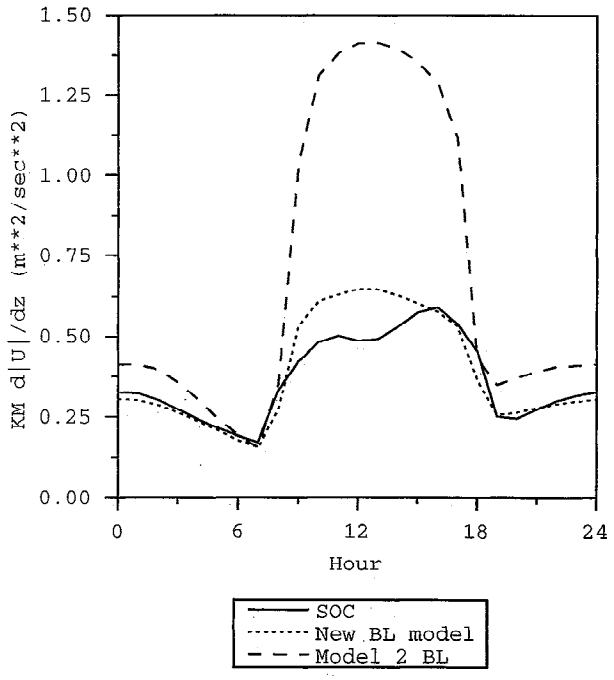

Figure 5. The diurnal variation of the momentum flux, $K_M\, d|U|/dz$, at the surface computed using the SOC model, the new BL model, and the Model 2 BL model in the off-line simulation.

It should be noted that the Ekman length computed for the Model 2 BL at hour 3 is 558.86 m and at hour 15 it is 3560.7 m. A large Ekman length is frequently a source of error with the Model 2 BL since the Ekman length is the only length scale in the model. If the BL height is larger than the Ekman length, the wind profiles are actually quite reasonable, although the consistently large values of K_M in the model tend to inhibit the turning of the wind as the altitude is decreased and force the surface wind to be too large. For situations in which the Ekman length is large compared to the boundary layer height, the model produces results that can only be described as terrible. It is worth noting that the present results are computed at a midlatitude. Off-line simulations at low latitudes have resulted in Ekman lengths in the Model 2 BL of the order of tens of kilometers, and the wind profile in the boundary layer is then essentially a straight vertical line on the scale of the plots presented here.

The fluxes and wind direction computed under unstable conditions with the new model, while much improved relative to the Model 2 BL, still show room for further improvement. The transport coefficients are seen to compare favorably to the SOC simulation, and the drag coefficient and Stanton numbers match the SOC results quite well (no surprise since they use the same formulation); however, the surface wind direction is not especially well matched by the SOC result. The reason for this is that most of the turning of the wind in the SOC simulation occurs fairly high up in the BL, where K_M is quite small. The new BL cannot capture this behavior using a constant value of K_M which is a compromise used to get the surface wind speed correct while maintaining a reasonable degree of wind turning.

It is clear that results generated using the new BL model agree much more favorably with the SOC simulation than do those of the Model 2 BL. The SOC model itself has been extensively tested against experimental data and seems to be the only way to easily provide a benchmark against which our BL models can be tested. It is also apparent that there are still weaknesses in the new model which need to be addressed in future versions; however, the new model goes a long way toward fixing some of the problems inherent in the Model 2 BL.

6. GCM Results

The new boundary layer was inserted into Model 2 of the GISS GCM [*Hansen et al.*, 1983]. The boundary layer is the only component of the model which has been changed; thus differences between the control run (Model 2 with the old boundary layer) and the new boundary layer experiment are due solely to the altered parameterizations given above. All comparisons, unless otherwise noted, are with the 4° × 5° version of the GCM; both experiment and control are run for 6 years, with results shown averaged over the last 5 years.

6.1. Local Effects of New Boundary Layer Formulation

To review the characteristic changes produced by the new boundary layer in an individual grid box, results are displayed from the Australian "desert," located at 26°S, 130°E, during January. While effects differ somewhat from grid box to grid box (they are less obvious over the ocean, for example), the nature of the changes in this location is indicative of the gen-

Table 1. Comparison of Some Results for Stable Conditions at Hour 3

	SOC	New BL	Model 2 BL
T_{surf}, K	284.29	284.97	284.48
U_{surf}, m/s	5.1961	5.3892	9.1296
V_{surf}, m/s	3.5237	3.2468	3.7273
Surface wind, m/s	6.2782	6.2916	9.8611
Wind turning, °	34.142	31.067	19.105
K_M, m^2/s	5.2183	5.0957	14.639
K_H, m^2/s	2.3055	1.4109	14.639
c_m	6.9290×10^{-3}	6.6506×10^{-3}	3.6655×10^{-3}
c_h	5.0361×10^{-3}	4.7933×10^{-3}	4.6010×10^{-3}
$K_M\, d\|U\|/dz$, m^2/s^2)	0.27311	0.26326	0.35644
$K_H\, dT/dz$, K m/s	4.3352×10^{-2}	6.1874×10^{-2}	7.1109×10^{-2}

The boundary layer height is 1075 m, the ground temperature is 282.92 K, and the temperature at 200 m is 285.41 K.

Table 2. Comparison of Some Results for Unstable Conditions at Hour 15

	SOC	New BL	Model 2 BL
T_{surf}, K	288.38	288.93	288.01
U_{surf}, m/s	7.6512	8.6257	13.134
V_{surf}, m/s	3.7547	1.7751	3.0378
Surface wind, m/s	8.5228	8.8064	13.481
Wind turning, °	26.139	11.629	2.0225
K_M, m^2/s	69.464	43.924	594.27
K_H, m^2/s	4.1928	3.5517	594.27
c_m	7.8967×10^{-3}	7.7728×10^{-3}	7.4503×10^{-3}
c_h	5.7785×10^{-3}	5.6929×10^{-3}	1.0298×10^{-2}
$K_M\, d\|U\|/dz$, m^2/s^2)	0.57385	0.60281	1.35394
$K_H\, dT/dz$ (K m/s)	-7.9641×10^{-2}	-5.3594×10^{-2}	−0.27650

The boundary layer height is 1558.3 m, the ground temperature is 290 K, and the temperature at 200 m is 287.92 K.

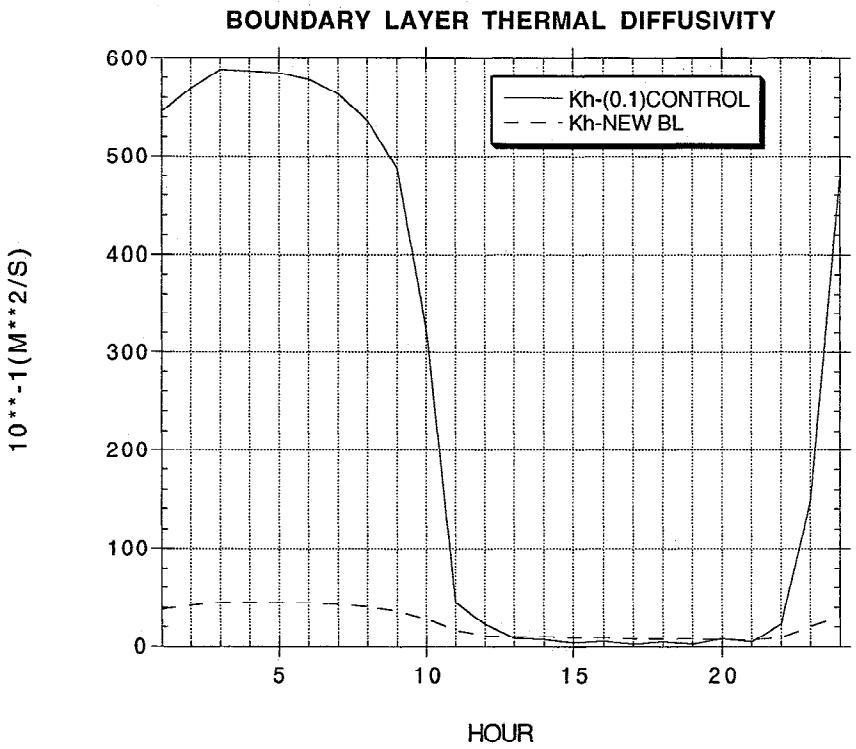

Figure 6. Diurnal variation of boundary layer thermal diffusivity (K_H) for the Australian desert grid box (26°S, 130°E) averaged over the month of January. Results are shown for the control run with the old boundary layer formulation (solid line) and with the new boundary layer (dashed line). Hours are UT. (Sunrise is 2100 UT.) Results are averages over 5 years.

eral response, and the instability generated during the afternoon highlights the more dramatic differences.

Shown in Figure 6 is the boundary layer turbulent diffusivity for heat (K_H) (as well as for moisture, since K_H is set equal to K_q) as a function of hour (UT), averaged over the month of January. (At this location and month, sunrise occurs at 2100 UT.) With the old boundary layer parameterization, the values of K_H are quite large: an order of magnitude greater than can be computed from observations for this location (e.g., the Wangara data of *Clarke et al.* [1971] and *Galperin et al.* [1988]) during the late afternoon. The new boundary layer formulation reduces the magnitude of the turbulent diffusivity under unstable conditions (equation (35), which can be compared with the old Richardson number formulation, equation (53) of *Hansen et al.* [1983]). The smaller values of turbulent diffusivity, as well as of turbulent viscosity, produce a greater turning of the wind from top to bottom of the boundary layer and can potentially alter the surface fluxes by forcing the surface temperature and specific humidity closer to the ground level values (compare (28) and (30), or (29) and (31)).

Figure 7 displays the surface drag coefficient and Stanton number. In both cases the new coefficients are about 1/3 of the old values during the sunlit hours, while the old value for c_h drops below the new value during stable conditions at night. The formulations for the new coefficients (equations (45)–(60)) have distinctly different stability scalings than those used by *Hansen et al.* [1983, equations (49)–(51)], which were simplifications of *Deardorff*'s [1967] approximations of the stability relations as functions of a bulk Richardson number. The reduced drag coefficient and Stanton number should lead to greater surface fluxes and frictional drag (equations (28), (29), and (44)).

The resultant surface fluxes are influenced by changes in the vertical transport coefficients as well as in the surface drag coefficient, Stanton number, and Dalton number (equations (28)–(31)). The hourly fluxes of heat and moisture are shown in Figure 8. The reduced drag coefficient from the new boundary layer has indeed resulted in a reduction in sensible heat flux during the unstable hours. The latent heat flux is essentially unchanged; ultimately, control over evaporation in a region in which potential evaporation exceeds precipitation depends mostly upon the magnitude of the precipitation, which was relatively unchanged in this region.

Alterations in the transport and drag coefficients, Stanton number, and Dalton number will also affect surface variables such as temperature, moisture, and wind (which will be discussed in the following section). Figures 9a and 9b display the low-level temperatures in the control run and the new boundary layer run, respectively. The surface air temperature should be between the ground temperature (i.e., the temperature at z_{0h} in the formalism presented here) and the first layer potential temperature (equations (28) and (30)) for both models. It is apparent that on the monthly average this was not the case in Model 2, probably due to numerical instabilities associated with the large transport coefficients. With the new boundary layer the problem is corrected. Note that the ground and surface air temperatures are warmer with the new boundary layer, due at least in part to the reduction in the Stanton number and sensible heat flux.

The new boundary layer has also produced a change in the

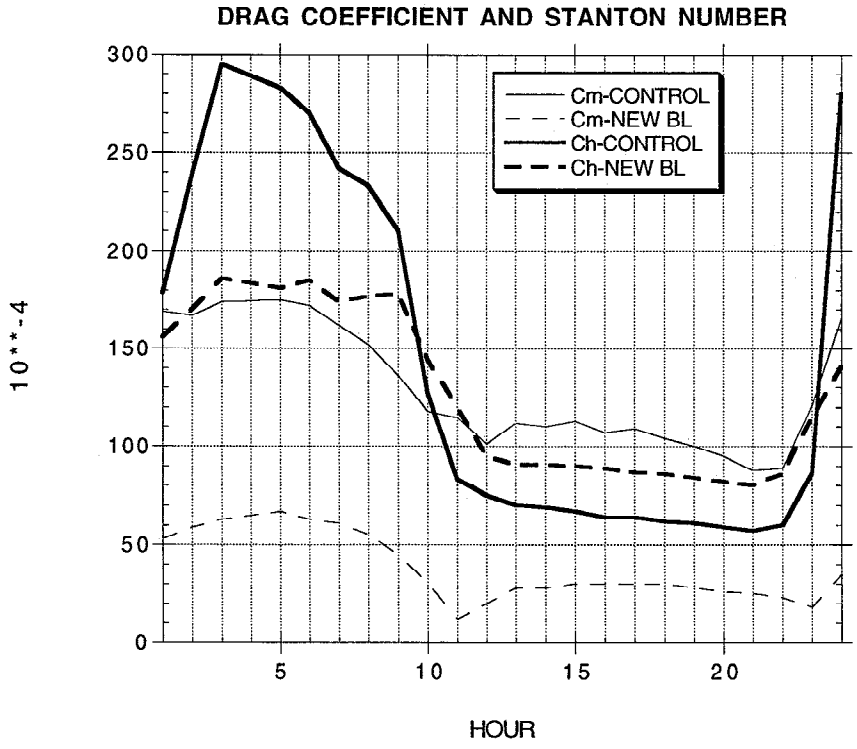

Figure 7. As in Figure 6, except for the drag coefficient (c_m) and the Stanton number (c_h).

diurnal temperature range. In the control run it was about 14°C, while with the new boundary layer it is now 16°C; this appears to be a real difference, since the interannual standard deviation is less than 1°C in this quantity. Observed values for this region [*May et al.*, 1992] are 12°–13°C; thus both models are too high, and in fact the new boundary layer model is somewhat worse. Overall, the mean temperature in January is several degrees too warm, whereas in the control run it was not. These results display that a more realistic representation of model physics does not necessarily result in a better match with the climatology. It must be kept in mind that other processes in the model influence the diurnal temperature range and mean surface air temperature, including the land surface parameterizations. Both boundary layer formulations are being run with an extremely simple land surface model. A new land surface model in the GISS GCM reduces both the diurnal range and the mean temperature [*Rosenzweig and Abramopolous*, 1997].

In Figure 10 are presented the variations of the surface and ground specific humidity (the ground value being the moisture in equilibrium with the soil moisture at the temperature of the ground). In the old model the very large transport coefficients during unstable time periods removed moisture from the surface layer extremely effectively, producing the odd result that

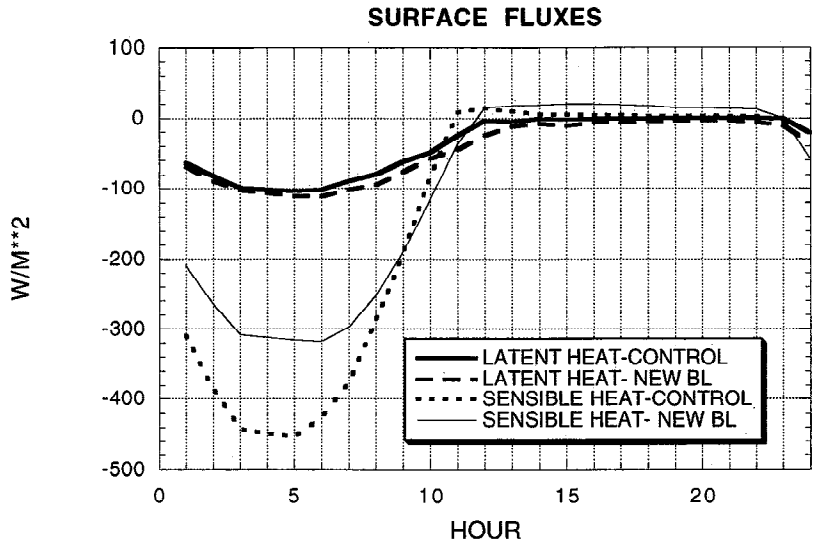

Figure 8. As in Figure 6, except for the latent and sensible heat fluxes.

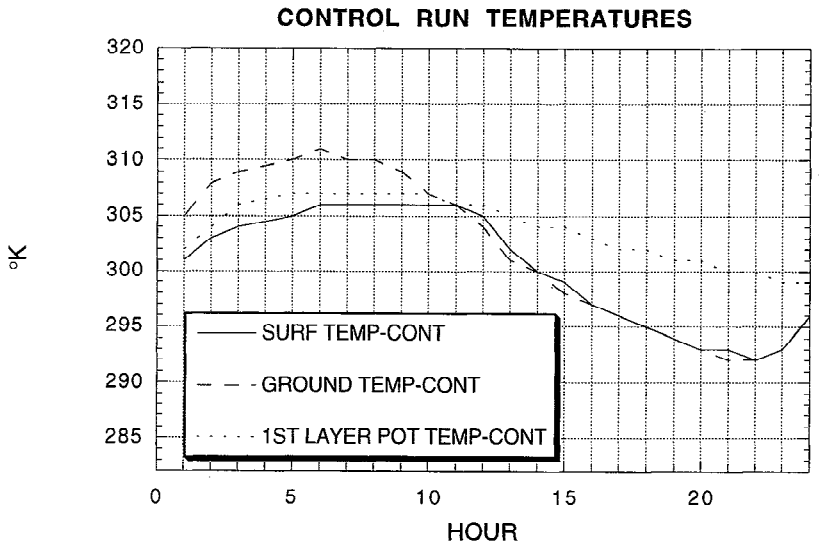

Figure 9a. Diurnal variation of ground temperature (first 10 cm of the ground), surface air temperature (at a height of 30 m), and potential temperature of the first layer (at approximately 960 mbar) in the control run with the old boundary layer.

there was less specific humidity near the surface when the surface air temperature was largest. With the new boundary layer this problem is once again corrected.

6.2. Global Effects of New Boundary Layer Formulation

By affecting local fluxes of heat, moisture, and momentum, a boundary layer formulation can also impact the global climate simulation. This aspect was discussed extensively by *Hansen et al.* [1983] (e.g., see Figure 7 of that paper). Here we discuss the large-scale changes wrought by the new boundary layer formulation.

The use of large transport coefficients and the mathematical inapplicability of the infinite depth Ekman solution at low latitudes both have an effect on the wind turning from the top to the bottom of the boundary layer. With the new boundary layer formulation the wind speed at low latitudes is greater by 0.5–1 m/s and there is greater convergence near 4°N. Both results increase the realism of the simulation; the equatorial winds of the model have been too weak [*Russell et al.*, 1995], and convergence should maximize near the equator [*Trenberth et al.*, 1989].

The resulting latent heat fluxes are shown in Figure 11 compared with observed values. Observations [from *Schutz and Gates*, 1971] are after *Budyko* [1963], generated from surface wind values and must therefore be considered approximate. The reduced values at low latitudes are somewhat more accurate, in particular north of the equator. The latent heat flux differences shown are significant; model interannual variability on the zonal average is of the order of 5 W/m^2.

Despite the increase in surface wind speed, the latent heat fluxes are smaller due to the reduced Dalton number. In fact, the model as a whole has reduced latent heat fluxes, globally on the order of 11%, which is a reduction in the flux of heat away from the surface of 10 W/m^2. In response, the surface air

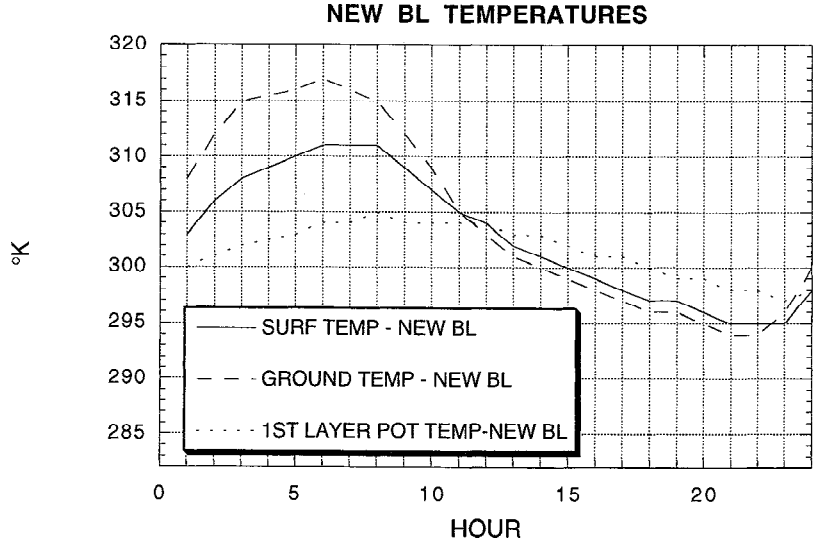

Figure 9b. As in Figure 9a, except for the new boundary layer run.

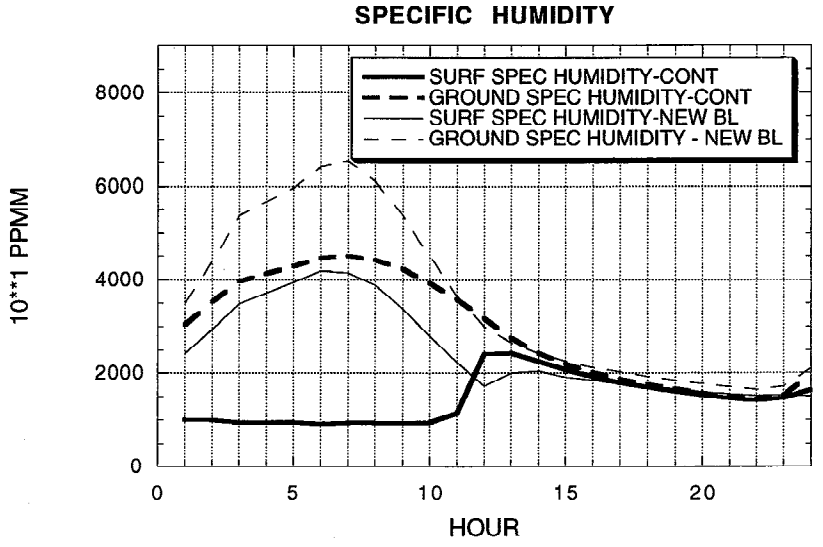

Figure 10. As in Figure 6, except for the specific humidity near the ground and at 30 m elevation.

temperature is 1°C warmer over land (consistent with the sign of the change noted above for the Australian desert).

The zonal average precipitation for January is presented in Figure 12. The new version of the model, with its greater equatorial convergence and the reduced evaporation north of the equator, has reduced the spuriously large northern hemisphere peak. This problem has been identified as causing the low interhemispheric transport in Model 2; with the new boundary layer (and new convection scheme), interhemispheric transport in the model now appears accurate [*Rind and Lerner*, 1996].

The geographic distribution of the precipitation change is given in Figure 13. Reductions in precipitation occur across a wide range of longitudes but are particularly evident in the Bay of Bengal and central American regions.

The zonal average precipitation for July is presented in Figure 14. The control run had excess precipitation south of the equator, and there is only slight improvement in the overall latitudinal distribution with the new boundary layer. Also shown are the results with the addition of a new convection scheme [*Del Genio and Yao*, 1992]. Further improvement is evident, although the model still overestimates precipitation in

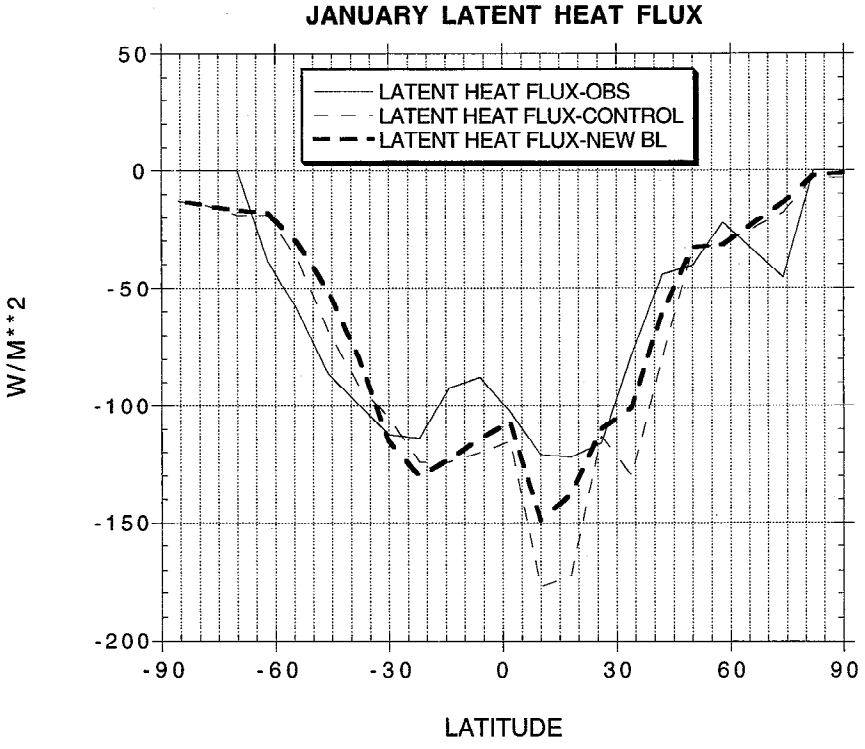

Figure 11. January latent heat flux as a function of latitude with the old and new boundary layer. Also shown are observations from *Schutz and Gates* [1971].

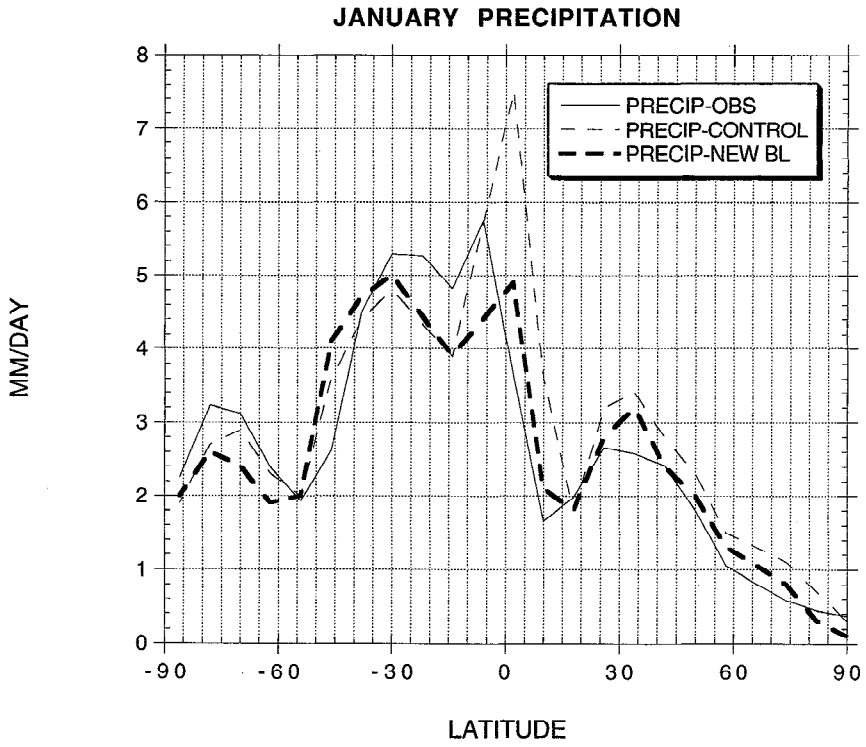

Figure 12. As in Figure 11, except for precipitation.

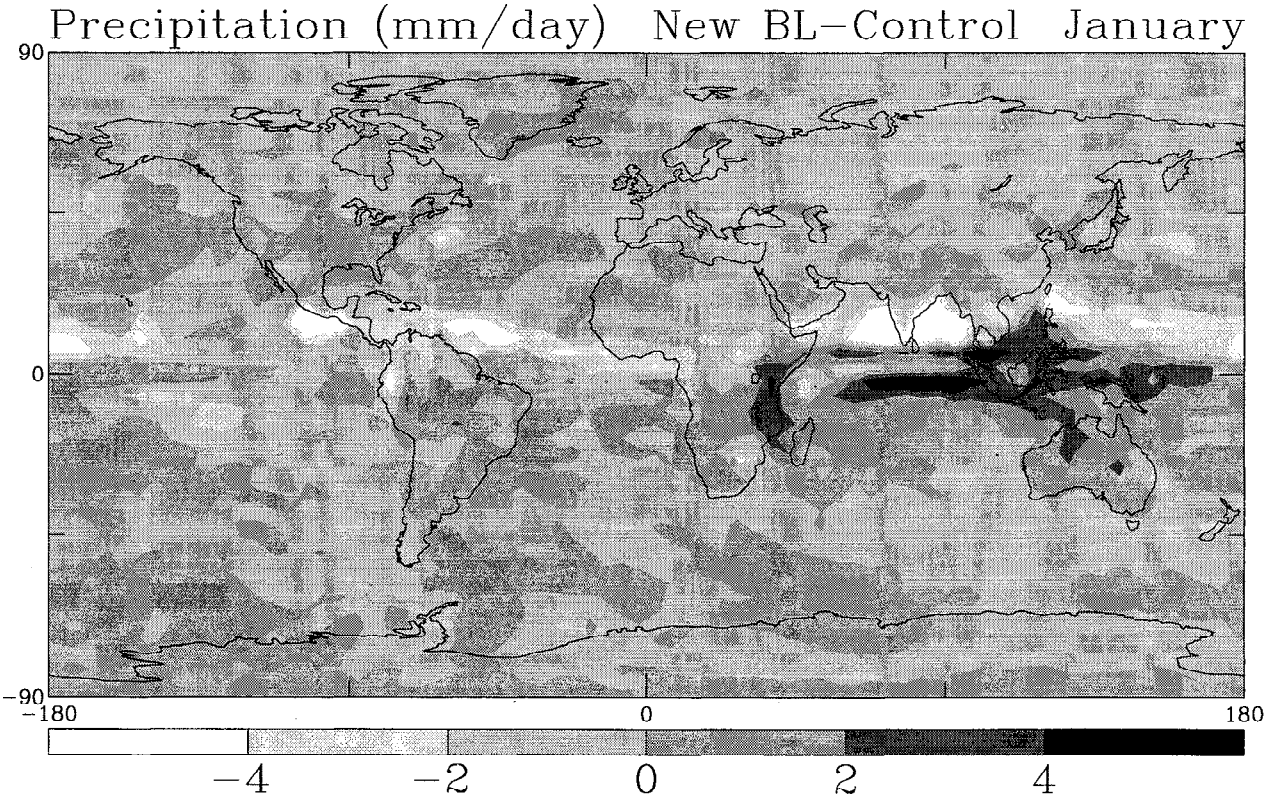

Figure 13. Distribution of rainfall change between the new boundary layer and control run simulations during January. Results are from 5-year simulations.

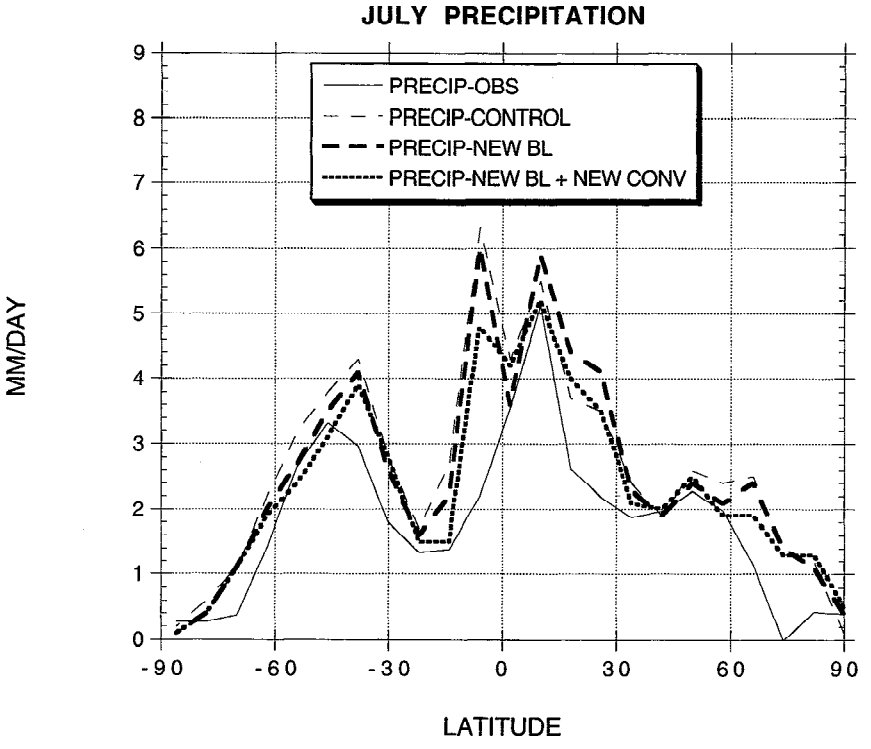

Figure 14. As in Figure 12, except for July.

the southern Pacific convergence zone. It should be noted that there are significant differences among observational data sets (e.g., the microwave sounding unit and rain gauge data sets) in this region and that many models appear to overestimate rainfall based on rain gauge estimates [*Sperber and Palmer*, 1995]. The apparently positive impact resulting from the new convection scheme emphasizes that dynamical influences on hydrological processes can result from various model parameterizations in nonstraightforward ways; as shown by *Rind and Lerner* [1996], the new convection did little to improve or alter the January rainfall distribution.

The new boundary layer has increased surface wind speed with a reduced surface momentum drag coefficient; therefore the effects on the total surface torque tend to compensate. This result is shown in Figure 15 where estimates of the observed surface torque on angular momentum are compared with experiments in which the new boundary layer is put into both 4° × 5° and 2° × 2.5° versions of the GCM. At both resolutions the effect of the new boundary layer is small. The global momentum budget is governed by numerous processes, including eddy transports of momentum, mountain torque, etc.; in both boundary layer parameterizations the winds and coefficients

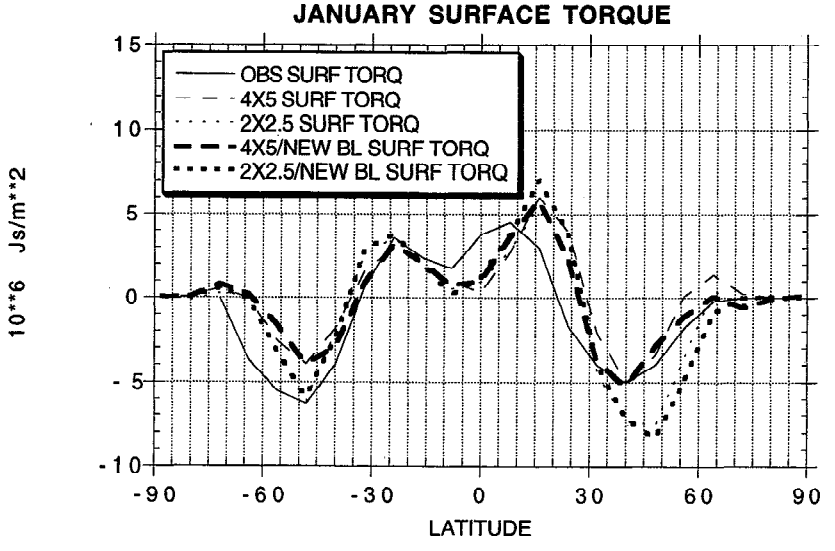

Figure 15. January surface torque for the old and new boundary layer experiments at both 4° × 5° and 2° × 2.5° resolutions. Also shown are observations from *Peixoto and Oort* [1992].

Table 3. Changes Produced by New Boundary Layer

Parameter	Change, %
Eddy kinetic energy	−8
Baroclinic eddy kinetic energy generation	−23
Peak northward transport of sensible heat (48°N)	−23
Northward transport of eddy energy by eddies	−12
Total atmospheric northward transport of energy	−11

respond to these other processes which have not been changed sufficiently to alter the total torque in any substantial manner. In contrast, the surface torque is consistently larger in the 2° × 2.5° model, as the dynamics appear to shift energy into the zonal mean flow, increasing the surface wind speeds by some 20% and surface torques by 40% due to this effect alone.

The boundary layer parameterization can apparently have a greater effect on kinetic energy, a result which has previously been discussed by *Hansen et al.* [1983]. Given in Table 3 are the changes in eddy energy, its generation and transports, and total atmospheric transports. The new boundary layer produces reductions in all these quantities with magnitudes generally twice the interannual standard deviation or greater. The actual change of kinetic energy by surface drag and dry convection is given in Figure 16. The increase in kinetic energy reduction is generally largest where the surface wind speed has increased. Additional energy reduction is associated with an increase of about 10% in dry convection (dry convection mixes momentum, which reduces kinetic energy). The increase in dry convection is due to the larger vertical gradient between the ground and first layer shown in Figure 9 (a result of the reduction in thermal diffusivity and Stanton number). The new total energy transport is in better agreement with observations, which seems to indicate that models produce greater than observed poleward energy fluxes [*Stone and Risbey*, 1990].

7. Discussion and Conclusions

The surface and boundary layer parameterizations used in the GISS model differ substantially from those used in any other GCM. The surface layer model presented here is quite sophisticated and is an attempt to compute the surface fluxes as accurately as possible. On the other hand, the new boundary layer model is evolutionary rather than revolutionary in that it retains the same methodology as that in Model 2: It attempts to circumvent the need for high resolution in this domain through an interpolation procedure that utilizes the more realistic aspects of similarity theory along with assumptions about wind turning with altitude. The new boundary layer model removes mistakes in the original Model 2 version yet remains much less sophisticated than extant schemes which resolve the boundary layer explicitly and solve directly for the prognostic variables. Nevertheless, the new boundary layer model is an improvement over that previously incorporated in Model 2, and the combination of a new surface layer model and an improved boundary layer model has resulted in distinct improvements in the climate depiction of the GISS GCM.

The goal of minimizing the impact on the execution time of the GISS GCM was attained through the use of extensive precomputation via look-up tables for the boundary layer properties. This actually resulted in an improvement of the order of 5–10% in the execution time relative to that of Model 2, an important consideration in a climate model that has been run for a simulation time up to a millenium.

The impact that the improvements of the surface and boundary layer parameterizations can have on local diurnal variations and large-scale processes has been depicted. Use of a modified finite depth Ekman layer and more realistic formulations for transport coefficients, drag coefficient, Stanton number, and Dalton number has improved both diurnal and latitudinal variations in various quantities. The diurnal variation of surface quantities is smoother and more realistic; the latitudinal variation of precipitation no longer shows the spurious northern hemisphere maximum in January. Effects of the order of 10–20% occur in eddy energy and transports. Clearly, accurate parameterizations of boundary layer processes will affect GCM simulations on all scales.

Using the new surface and boundary layer models, the climate depiction of the GISS GCM has certainly improved, but

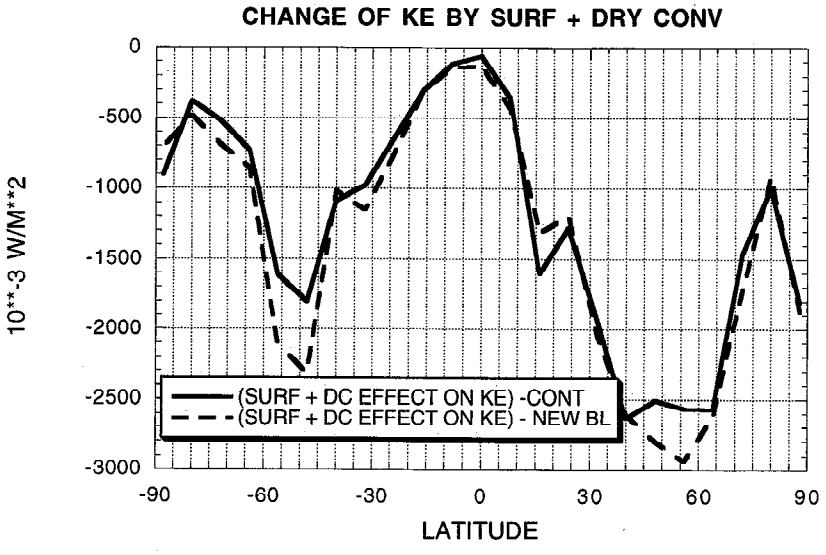

Figure 16. Change in kinetic energy (KE) during January by surface drag (SURF) and dry convection (DC) (through momentum mixing) for the control run and new boundary layer simulations.

it appears that further improvement is indeed desirable. Obviously, the current boundary layer model is an attempt to circumvent the lack of vertical resolution that seems inevitable in a GCM. There remain significant approximations whose impacts are difficult to assess for the large parameter space that is accessed by a GCM. In an effort to remove many of the approximations presented here, we are currently working to incorporate a second-order closure model as a sub–grid scale model to provide the turbulent transport of momentum, heat, and moisture between the ground and first model layer. The prototype uses the level 2 version of the SOC model of *Galperin et al.* [1988] to solve full prognostic equations for the mean fields on eight sublevels between the surface and first model layer. The surface layer formulation presented here is retained, and no geostrophic approximation need be introduced since the appropriate horizontal pressure gradients can be computed directly from the GCM. This prototype model for the GISS GCM currently requires approximately 2.5 times as long to execute each boundary layer time step as the model presented here, increasing the execution time of the GCM by about 15%.

Acknowledgments. The authors would like to thank Dan Kowalski and Hanspeter Zinn for helpful discussions during the development phases of this work and Barbara Carlson and Andy Lacis for providing the IBM RISC/6000 workstation on which the initial numerical development was done. This work was supported by the NASA Climate Modeling Program Office and the NASA Atmospheric Chemistry Modeling and Analysis Program.

References

Brutsaert, W. H., *Evaporation Into the Atmosphere*, D. Reidel, Norwell, Mass., 1982.

Budyko, M. I., *Atlas of the Heat Balance of the Earth*, Gidrometeorizdat, Moscow, 1963.

Clarke, R. M., A. J. Dyer, R. R. Brook, D. G. Reid, and A. J. Troup, The Wangara Experiment: Boundary layer data, *Tech. Pap. 10*, Div. of Meteorol. Phys., Commonw. Sci. and Ind. Res. Organ., Melbourne, Victoria, Australia, 1971.

Deardorff, J. W., Empirical dependence of the eddy coefficient for heat upon stability above the lowest 50 m, *J. Appl. Meteorol.*, *6*, 631–643, 1967.

Del Genio, A. D., and M.-S. Yao, Efficient cumulus parameterization for long-term climate studies: The GISS scheme, in *Cumulus Parameterization, AMS Monogr. Ser.*, vol. 24, edited by K. Emanuel and D. Raymond, 181–184, Am. Meteorol. Soc., Boston, Mass., 1992.

Galperin, B., L. H. Kantha, S. Hassid, and A. Rosati, A quasi-equilibrium turbulent energy model for geophysical flows, *J. Atmos. Sci.*, *45*, 55–62, 1988.

Garratt, J. R., Sensitivity of climate simulations to land-surface and atmospheric boundary-layer treatments—A review, *J. Clim.*, *6*, 419–449, 1993.

Hansen, J., G. Russell, D. Rind, P. Stone, A. Lacis, S. Lebedeff, R. Ruedy, and L. Travis, Efficient three-dimensional global models for climate studies: Models I and II, *Mon. Weather Rev.*, *111*, 609–662, 1983.

Hogstrom, U., Non-dimensional wind and temperature profiles in the atmospheric surface layer: A re-evaluation, *Boundary Layer Meteorol.*, *42*, 55–78, 1988.

May, W., D. J. Shea, and R. A. Madden, The annual variation of surface temperatures over the world, *NCAR Tech. Note, TN-372+STR*, 145 pp., 1992.

Monin, A. S., and A. M. Yaglom, *Statistical Fluid Mechanics: Mechanics of Turbulence*, vol. 1, edited by J. L. Lumley, MIT Press, Cambridge, Mass., 1971.

Pedlosky, J., *Geophysical Fluid Dynamics*, Springer-Verlag, New York, 1979.

Peixoto, J. P., and A. H. Oort, *Physics of Climate*, Am. Inst. of Phys., New York, 1992.

Rind, D., and J. Lerner, Use of on-line tracers as a diagnostic tool in general circulation model development, *J. Geophys. Res.*, *101*, 12,667–12,683, 1996.

Rosenzweig, C., and F. Abramopoulos, Land-surface model development for the GISS GCM, *J. Clim.*, in press, 1997.

Russell, G. L., J. Miller, and D. Rind, A coupled atmosphere-ocean model for transient climate studies, *Atmos. Oceans*, *33*, 683–730, 1995.

Schutz, C., and W. L. Gates, Global climatic data for surface, 800 mb, 400 mb: January, *Rand Rep. R-915-ARPA*, Adv. Res. Proj. Agency, Dep. of Def., Washington, D. C., 1971.

Sperber, K. R., and T. N. Palmer, Interannual tropical rainfall variability in general circulation model simulations associated with the Atmospheric Model Intercomparison Project, *PCMDI Rep. 28*, 79 pp., Lawrence Livermore Natl. Lab., Univ. of Calif., Livermore, 1995.

Stone, P., and J. S. Risbey, On the limitations of general circulation models, *Geophys. Res. Lett.*, *17*, 2173–2176, 1990.

Taylor, G. I., Eddy motion in the atmosphere, *Philos. Trans. R. Soc. London, Ser. A*, *215*, 1–26, 1915.

Taylor, G. I., Skin friction of the wind on the Earth's surface, *Proc. R. Soc. London, Ser. A*, *92*, 196–199, 1916.

Trenberth, K. E., J. G. Olson, and W. G. Large, A global wind stress climatology based on the ECMWF analyses, *NCAR Tech. Note, TN-338-STR*, 93 pp., 1989.

Yamada, T., On the similarity functions A, B and C of the planetary boundary layer, *J. Atmos. Sci.*, *33*, 781–793, 1976.

G. J. Hartke, Center for Climate Systems Research, Columbia University, 2880 Broadway, New York, NY 10025. (e-mail: ghartke@giss.nasa.gov)

D. Rind, Institute for Space Studies, NASA Goddard Space Flight Center, 2880 Broadway, New York, NY 10025.

(Received August 16, 1996; revised December 12, 1996; accepted March 4, 1997.)